
Spectral Informed Neural Network: An Efficient and Low-Memory PINN

Tianchi Yu*

Skolkovo Institute
of Science and Technology
Tianchi.Yu@skoltech.ru

Yiming Qi*

Peking University
2001111682@stu.pku.edu.cn

Ivan Oseledets

AIRI;
Skolkovo Institute
of Science and Technology
I.Oseledets@skoltech.ru

Shiyi Chen

Peking University;
Southern University
of Science and Technology
chensy@sustech.edu.cn

Abstract

With growing investigations into solving partial differential equations by physics-informed neural networks (PINNs), more accurate and efficient PINNs are required to meet the practical demands of scientific computing. One bottleneck of current PINNs is computing the high-order derivatives via automatic differentiation which often necessitates substantial computing resources. In this paper, we focus on removing the automatic differentiation of the spatial derivatives and propose a spectral-based neural network that substitutes the differential operator with a multiplication. Compared to the PINNs, our approach requires lower memory and shorter training time. Thanks to the exponential convergence of the spectral basis, our approach is more accurate. Moreover, to handle the different situations between physics domain and spectral domain, we provide two strategies to train networks by their spectral information. Through a series of comprehensive experiments, We validate the aforementioned merits of our proposed network.

1 Introduction

With the rapid advancements in machine learning and its related theories, integrating mathematical models with neural networks provides a novel framework for embedding physical laws in scientific research. The representative methods are the Physics-Informed Neural Networks (PINNs) [1] and the Deep Ritz method [2]. PINNs have garnered significant attention because of their ability of solving partial differential equations (PDEs) without suffering from the curse of dimensionality (CoD) [3, 4], thanks to the Monte Carlo method [5], automatic differentiation (AD) [6], and universal approximation theorem [7]. Additionally, PINNs demonstrate the merits in handling imperfect data [8], extrapolation [9, 10], and interpolation [11]. These capabilities have propelled PINNs into a wide applications, including but not limited to fluid dynamics [12], aerodynamics [13], surface physics [14], power systems [15], and heat transfer [16].

However, using AD to compute the loss function (mainly the residual term) during training, is inefficient and computational expensive. To address this problem, various approaches have been proposed that leverage alternative numerical methods to replace AD. For instance, PhyCRNet [10, 17] utilizes the finite difference method (FDM) to replace AD; DTPINN [18] applies the finite difference

*Equal contribution

for radial basis functions instead of high-order derivatives; sPINN [19] employs the spectral method of orthogonal polynomials to avoid computing the derivatives and Spectral PINNs [20] utilize Hermite polynomials for uncertainty quantification. On the other hand, some researchers focus on improving the efficiency of AD, the representative method is the Taylor-mode [21].

Unfortunately, directly embedding those conventional numerical methods into PINNs will resuffer the CoD. However, the spectral method offers a promising alternative by approximating solutions within the spectral domain. By mapping sampled frequencies to their corresponding coefficients, the spectral method can be embedded into PINNs in a manner that circumvents the CoD. sPINNs have utilized a similar idea in their implementation of the spectral method; nevertheless, they only illustrate a few experiments of linear PDEs on finite, semi-infinite, and infinite intervals with truncated Chebyshev polynomials, Laguerre polynomials, and Hermite polynomials, respectively. Technically speaking, when considering non-linear PDEs, aliasing errors caused by nonlinear terms should be suppressed in the spectral domain via dealiasing operations. While in sPINNs, they didn't discuss it. Furthermore, their input is the spatial and temporal grid points, which makes sPINNs unable to fully exploit the mesh-free features of spectral methods and adaptively sample from the frequencies.

In this paper, we propose the Spectral-Informed Neural Networks (SINNs) as an efficient and low-memory approach to train networks for the PDEs with periodic boundary conditions by the spectral information based on Fourier basis. Compared to PINNs, our SINNs utilize a precise and efficient alternative to AD to acquire spatial derivatives; the input is the frequencies of the Fourier basis rather than the grid points from the physics domain, and the output is the coefficients in the spectral domain rather than the physical solution. Furthermore, the merit of the exponential convergence for approaching any smooth function [22] not only makes spectral methods achieved superior accuracy in traditional computational science [22, 23], but it also enables SINNs to achieve smaller errors.

Our specific contributions can be summarized as follows:

1. We propose a method that tackles the spatial derivatives of the network to deal with the high GPU memory consumption of PINNs.
2. We propose two strategies to approximate more of the primary features in the spectral domain by learning the low-frequency preferentially to handle the difference between SINNs and PINNs.
3. Our experiments show that the method can reduce the training time and improve the accuracy simultaneously.

The paper is structured as follows: In Section 2, we provide a concise overview of PINNs and discuss AD and its developments. Using a simple experiment, we highlight the challenge encountered in computing high-order derivatives within PINNs. To address this drawback, in Section 3, we propose our SINNs and give an intuitive understanding with two examples. In Section 4, we demonstrate state-of-the-art results across a comprehensive experiment. Finally, Section 5 provides a summary of our main research and touches upon remaining limitations and directions for future research.

2 Physics-informed neural networks (PINNs)

We briefly review the physics-informed neural networks (PINNs) [1] in the context of inferring the solutions of PDEs. Generally, we consider PDEs for \mathbf{u} taking the form

$$\begin{aligned} \partial_t \mathbf{u} + \mathcal{N}[\mathbf{u}] &= 0, \quad t \in [0, T], \mathbf{x} \in \Omega, \\ \mathbf{u}(0, \mathbf{x}) &= \mathbf{g}(\mathbf{x}), \quad \mathbf{x} \in \Omega, \\ \mathcal{B}[\mathbf{u}] &= 0, \quad t \in [0, T], \mathbf{x} \in \partial\Omega, \end{aligned} \tag{1}$$

where \mathcal{N} is the differential operator, Ω is the domain of grid points, and \mathcal{B} is the boundary operator.

The ambition of PINNs is to obtain the unknown solution \mathbf{u} to the PDE system Eq. (1), by a neural network \mathbf{u}^θ , where θ denotes the parameters of the neural network. The constructed loss function is:

$$\mathcal{L}(\theta) = \mathcal{L}_{ic}(\theta) + \mathcal{L}_{bc}(\theta) + \mathcal{L}_r(\theta), \tag{2}$$

where

$$\begin{aligned}\mathcal{L}_r(\theta) &= \frac{1}{N_r} \sum_{i=1}^{N_r} |\partial_t \mathbf{u}^\theta(t_r^i, \mathbf{x}_r^i) + \mathcal{N}[\mathbf{u}^\theta](t_r^i, \mathbf{x}_r^i)|^2, \\ \mathcal{L}_{ic}(\theta) &= \frac{1}{N_{ic}} \sum_{i=1}^{N_{ic}} |\mathbf{u}^\theta(0, \mathbf{x}_{ic}^i) - \mathbf{g}(\mathbf{x}_{ic}^i)|^2, \\ \mathcal{L}_{bc}(\theta) &= \frac{1}{N_{bc}} \sum_{i=1}^{N_{bc}} |\mathcal{B}[\mathbf{u}^\theta](t_{bc}^i, \mathbf{x}_{bc}^i)|^2,\end{aligned}\tag{3}$$

corresponds to the three equations in Eq. (1) individually; $\mathbf{x}_{ic}^i, \mathbf{x}_{bc}^i, \mathbf{x}_r^i$ are the sampled points from initial constraint, the boundary constraint, and the residual constraint; N_{ic}, N_{bc}, N_r are the total number of sampled points correspondingly.

2.1 Automatic differentiation (AD)

AD gives the required derivative of an overall function by combining the derivatives of the constituent operations through the chain rule based on evaluation traces. Herein, AD is used to calculate the derivatives respect to the input points in PINNs. However, AD demands both memory and computation that scale exponentially with the order of derivatives (Fig. 1(a)) although there are investigations [21, 24, 25] on computing high-order derivatives efficiently by Faà di Bruno’s formula². Alternatively, replacing the high-order derivatives by simple multiplication, SINNs can reduce both memory and training time (Fig. 1(a) and Table 3).

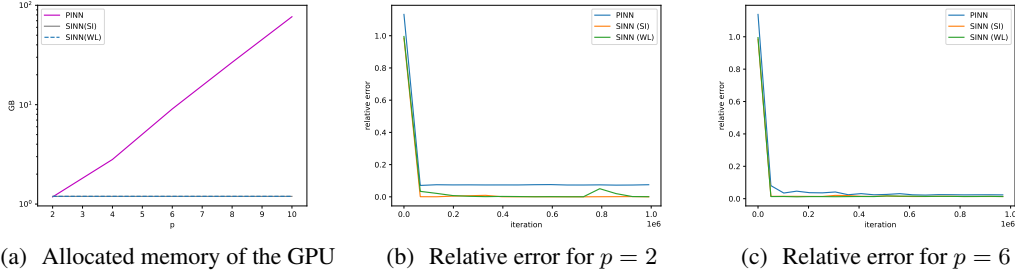


Figure 1: In the experiments for Eq. (24) with different p , (a) depicts the measured maximum memory of the GPU allocated during training, implying that the memory increases exponentially with p for the spatial derivative $\partial^p u / \partial x^p$ in PINNs and is constant for the multiplication $k^p \hat{u}$ in SINNs. And the corresponding relative L2 errors with iterations for $u(t = 0.1, x)$ are shown in (b) and (c) for $p = 2, p = 6$ respectively, indicating that SINNs are more accurate than PINNs whatever dealing with low-order derivatives or high-order derivatives. The further discussion of the experiments is presented in Section 4.1.

3 Spectral Information Neural Networks (SINNs)

To implement spectral method into PINNs, the Fourier operator \mathcal{F} is applied to Eq. (1), converting the solution from physics domain to the frequency domain. Practically, we use \mathcal{F}_N to represent the N -th truncated Fourier operator:

$$\mathcal{F}_N[u](t, x) = \sum_{k=-N/2}^{N/2-1} \hat{u}(t, k) e^{ikx},\tag{4}$$

²the further discussion is in Appendix A

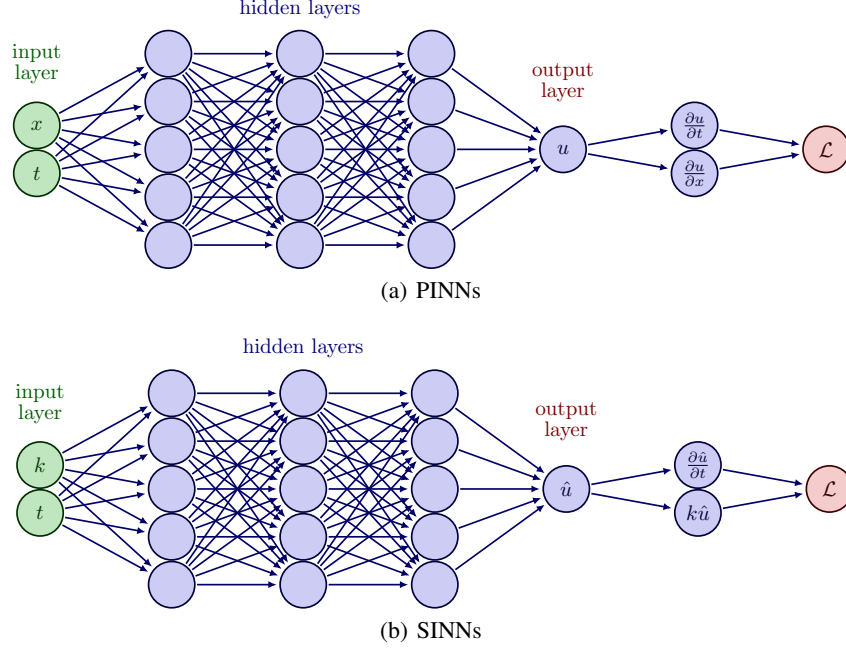


Figure 2: Comparison of PINNs and SINNs. In PINNs, the input is the spatial and temporal grid points from the domain, the output is the physical solution u . In SINNs, the input is the frequencies of the Fourier basis and the temporal grid points from the domain, the output is the coefficients \hat{u} in the spectral domain.

where \hat{u} corresponds to the Fourier coefficients of u , and $i \equiv \sqrt{-1}$ is the unit imaginary number. One can easily obtain the following derivatives:

$$\partial_t \mathcal{F}_N[u](t, x) = \sum_{k=-N/2}^{N/2-1} \partial_t \hat{u}(t, k) e^{ikx}, \quad (5)$$

$$\partial_x \mathcal{F}_N[u](t, x) = \sum_{k=-N/2}^{N/2-1} ik \hat{u}(t, k) e^{ikx}. \quad (6)$$

Equation (6) straightforwardly shows the vanishment of the AD for spacial derivatives in spectral domain. To demonstrate how SINNs work intuitively, we study two representative examples, including a two-dimensional (2-D) heat equation (linear) and a 2-D Navier-Stokes (NS) equation (non-linear).

3.1 Physical model for heat transfer

Ideally, the heat transfer can be described by the heat equation which is investigated widely in mathematics as one of the prototypical PDEs. Given $\Omega \subset \mathbb{R}^2$, consider the 2-D heat equation with periodic boundary condition:

$$\begin{aligned} \partial_t u(t, \mathbf{x}) &= \partial_{xx} u(t, \mathbf{x}) + \partial_{yy} u(t, \mathbf{x}), \quad t \in [0, T], \mathbf{x} \in \Omega, \\ u(0, \mathbf{x}) &= \mathbf{g}(\mathbf{x}), \quad \mathbf{x} \in \Omega. \end{aligned} \quad (7)$$

When applying on the loss function Eq. (2), the residual loss $\mathcal{L}_r(\theta)$ is explicitly expressed by:

$$\mathcal{L}_r(\theta) = \frac{1}{N_r} \sum_{i=1}^{N_r} \left| \partial_t u^\theta(t_r^i, \mathbf{x}_r^i) - \partial_{xx} u^\theta(t_r^i, \mathbf{x}_r^i) - \partial_{yy} u^\theta(t_r^i, \mathbf{x}_r^i) \right|^2, \quad (8)$$

In our SINNs, the loss function is in spectral domain without the boundary constraint due to the periodic nature of the Fourier basis and the loss function $\mathcal{L}(\theta)$ is modified to:

$$\tilde{\mathcal{L}}(\theta) = \tilde{\mathcal{L}}_{ic}(\theta) + \tilde{\mathcal{L}}_r(\theta), \quad (9)$$

where

$$\tilde{\mathcal{L}}_r(\theta) = \frac{1}{N_r} \sum_{i=1}^{N_r} \left| \partial_t \hat{u}^\theta(t_r^i, \mathbf{k}^i) + (k_x^i)^2 \hat{u}^\theta(t_r^i, \mathbf{k}^i) + (k_y^i)^2 \hat{u}^\theta(t_r^i, \mathbf{k}^i) \right|^2, \quad (10)$$

$$\tilde{\mathcal{L}}_{ic}(\theta) = \frac{1}{N_{ic}} \sum_{i=1}^{N_{ic}} \left| \hat{u}^\theta(0, \mathbf{k}^i) - \mathbf{g}(\mathbf{k}^i) \right|^2,$$

and $\mathbf{k}^i = (k_x^i, k_y^i) \in [-N/2, N/2 - 1]^2$ is the sampled frequency from spectral domain.

3.2 Physical model for incompressible flows

The mathematical model describing incompressible flows is the incompressible NS equation, namely,

$$\nabla \cdot \mathbf{u} = 0, \quad t \in [0, T], \quad \mathbf{x} \in \Omega, \quad (11a)$$

$$\partial_t \mathbf{u} + \mathbf{u} \cdot \nabla \mathbf{u} = -\nabla p + \nu \Delta \mathbf{u}, \quad t \in [0, T], \quad \mathbf{x} \in \Omega, \quad (11b)$$

$$\mathbf{u}(0, \mathbf{x}) = \mathbf{g}(\mathbf{x}), \quad \mathbf{x} \in \Omega, \quad (11c)$$

where $\nabla = (\partial_x, \partial_y)$ is the gradient operator, $\mathbf{u}(t, \mathbf{x}) = (u, v)$ is the hydrodynamic velocity, $p(t, \mathbf{x})$ is the mechanical pressure, $\Delta = \nabla \cdot \nabla$ is the Laplace operator, and ν is kinematic viscosity. By Fourier transform and appropriate derivation tricks (see Appendix D), the continuity equation Eq. (11a) and momentum equation Eq. (11b) can be expressed in the spectral domain:

$$\mathbf{k} \cdot \hat{\mathbf{u}} = 0, \quad (12a)$$

$$\partial_t \hat{\mathbf{u}} = - \left(1 - \frac{\mathbf{k}\mathbf{k}\cdot}{|\mathbf{k}|^2} \right) \hat{\mathcal{N}} - \nu |\mathbf{k}|^2 \hat{\mathbf{u}}, \quad (12b)$$

where $|\mathbf{k}|^2 = \mathbf{k} \cdot \mathbf{k}$ is the inner product for $\mathbf{k} = (k_x, k_y)$, and $\hat{\mathcal{N}}$ is the non-linear term in the spectral domain, which has the rotational form $\mathcal{N} = (\nabla \times \mathbf{u}) \times \mathbf{u}$ in the physical space [22]. The continuity equation Eq. (12a) can be preserved strictly by the projection in our SINNs³; however, the non-linear term has the challenge of dealing with the aliasing error, which will be further discussed in Appendix B. After solving the aliasing error, the loss function is

$$\tilde{\mathcal{L}}_r(\theta) = \frac{1}{N_r} \sum_{i=1}^{N_r} \left| \mathcal{F}^{-1}[\partial_t \hat{\mathbf{u}}(t_r^i, \mathbf{k})] + \mathcal{F}^{-1} \left[\left(1 - \frac{\mathbf{k}\mathbf{k}\cdot}{|\mathbf{k}|^2} \right) \hat{\mathcal{N}}(t_r^i, \mathbf{k}) \right] + \nu \mathcal{F}^{-1} [|\mathbf{k}|^2 \hat{\mathbf{u}}(t_r^i, \mathbf{k})] \right|^2. \quad (13)$$

3.3 Importance optimisation

Compared to PINNs, the main divergence is the importance of different input points. Although the literature on sampling method [26, 27, 28] shows that the importance of the input points in physics domain can be dependent on the corresponding residual, generally speaking, every point is equally important without any prior knowledge. But for SINNs, normally the importance decreases as the corresponding frequency increases. For instance, the energy spectrum in the inertial ranges of 2-D turbulence (described by the 2-D NS equation) satisfies the scaling relation [29]:

$$\sum_{n-\frac{1}{2} \leq |\mathbf{k}| < n+\frac{1}{2}} |\hat{\mathbf{u}}(t, \mathbf{k})|^2 \sim n^{-3}. \quad (14)$$

Similar physical analysis can be performed for 1-D problems, and the physical background demonstrates that the Fourier coefficient $\hat{\mathbf{u}}$ decreases rapidly as an increase in frequency due to the effect of viscosity. In practical, comprehensive experiments in Fourier Neural Operator [30] show that the truncated Fourier modes can contain most features of the PDEs. Herein, PINNs learn every input point equally, while SINNs are supposed to learn the low-frequency points preferentially. To train the network based on the aforementioned divergence, we propose two strategies:

Sampling by importance (SI): Suppose $p(\mathbf{k})$ is the probability density function (PDF) used to sample the residual points, then the $p(\mathbf{k})$ in sampling by importance is defined as:

$$p(\mathbf{k}) \propto \frac{1}{\|\mathbf{k}\|_1 + \beta} + \alpha, \quad (15)$$

³There are many approaches to do such kind of projection, in this paper, we choose $\hat{\mathbf{u}} = (1 - \frac{\mathbf{k}\mathbf{k}\cdot}{|\mathbf{k}|^2}) \cdot \hat{\mathbf{u}}$.

where α, β are two hyperparameters. This PDF makes us sample more points on the low frequencies and less points on the high frequencies.

Weighted residual loss (WL): However, although the capability of the neural network is hard to estimate, we should exploit it as much as possible. In SI, training SINNs with high-frequencies is in pretty low possibilities, such kind of strategy makes network can't learn high-frequencies even if the constructed network can learn both low-frequencies and high-frequencies. To address this dilemma, inspired by the CausalPINN[31] and taking the 2-D heat equation as an example, we propose the weighted loss function⁴:

$$\tilde{\mathcal{L}}_r(\theta) = \frac{1}{M} \sum_{i=0}^M \exp\left(-\epsilon \sum_{k=0}^{i-1} \mathcal{L}_r^k\right) \mathcal{L}_r^i, \quad (16)$$

where

$$\mathcal{L}_r^i = \sum_{\|\mathbf{k}\|_1=i} \left| \partial_t \hat{u}^\theta(t_r, \mathbf{k}) + (k_x)^2 \hat{u}^\theta(t_r, \mathbf{k}) + (k_y)^2 \hat{u}^\theta(t_r, \mathbf{k}) \right|^2, \quad (17)$$

ϵ is the hyperparameter, and $M = \max(\|\mathbf{k}\|_1)$. Note that when solving on non-linear PDEs, the inverse operator requires the accurate coefficients of frequencies but the WL gives a different weight on different frequency. Herein WL can't be applied on non-linear PDEs.

3.4 Spectral convergence

Regardless of the convergence analysis in temporal domain⁵, assume that the capability of MLP is powerful enough, $u \in C^\infty(\Omega, \mathbb{R})$ is a smooth function from a subset Ω of a Euclidean \mathbb{R} space to a Euclidean space \mathbb{R} , and N is the number of discretized points.

Firstly, let's review the convergence rate of PINNs. Suppose u^* is the exact solution in the domain Ω and

$$\begin{aligned} \theta^* &\triangleq \arg \min_{\theta} \int_{\Omega} \mathcal{L}_r[u^\theta(x)] dx, \\ \theta_N^* &\triangleq \arg \min_{\theta} \sum_{i=1}^N \mathcal{L}_r[u^\theta(x_i)]. \end{aligned} \quad (18)$$

Then

$$\|u^{\theta_N^*} - u^*\|_{\Omega} \leq \underbrace{\|u^{\theta_N^*} - u^{\theta^*}\|_{\Omega}}_{\text{statistical error}} + \underbrace{\|u^{\theta^*} - u^*\|_{\Omega}}_{\text{approximation error}}, \quad (19)$$

where approximation error depends on the capability of PINNs. As the capability of MLP is powerful enough, $\|u^{\theta^*} - u^*\|_{\Omega} \ll \|u^{\theta_N^*} - u^{\theta^*}\|_{\Omega}$. Additionally, based on the Monte Carlo method, the statistical error is $\mathcal{O}(N^{-1/2})$ [32], then:

$$\|u^{\theta_N^*} - u^*\|_{\Omega} = \mathcal{O}(N^{-1/2}). \quad (20)$$

As for SINNs, with N discretized points, the truncated u^* is $u_N^* = \sum_{k=-N/2}^{N/2-1} \hat{u}^*(k) e^{ikx}$, suppose

$$\tilde{\theta}_N^* \triangleq \arg \min_{\theta} \sum_{i=1}^N \tilde{\mathcal{L}}_r[\hat{u}^\theta(k_i)]. \quad (21)$$

Then

$$\|u^{\tilde{\theta}_N^*} - u^*\|_{\Omega} \leq \underbrace{\|u^{\tilde{\theta}_N^*} - u_N^*\|_{\Omega}}_{\text{spectral error}} + \|u_N^* - u^*\|_{\Omega} \quad (22)$$

As the capability of MLP is powerful enough, $\|u^{\tilde{\theta}_N^*} - u_N^*\|_{\Omega} \leq \sum_{k=-N/2}^{N/2-1} \|\hat{u}^{\tilde{\theta}_N^*}(k) - \hat{u}^*(k)\| = 0$. Furthermore, as the spectral error is exponential convergence [22], then:

$$\|u^{\tilde{\theta}_N^*} - u^*\|_{\Omega} = o(N^{-s}), \quad \forall s > 0. \quad (23)$$

Thus, the convergence rate of SINNs is $o(N^{-s})$ for any $s > 0$ while the convergence rate of PINNs is $\mathcal{O}(N^{-1/2})$.

⁴Although the weighted residual loss looks complicated, it can be simplified (See Appendix E)

⁵Generally, the temporal error is always much smaller than spatial error so we can ignore the temporal error.

4 Experiments

To demonstrate the performance of the proposed SINNs, we consider training the linear equations (Table 1) using the framework shown in Section 3.1 and training the non-linear equations (Table 2) using the framework shown in Section 3.2. The details of the equations and training are available in Appendix C, the details of the relative L2 error metric used in our experiments are described in Appendix C.3.

Table 1: Comparison of the relative errors for the linear equations

equation	PINN	SINN (SI)	SINN (WL)
1-D convection-diffusion	u	$1.79 \times 10^{-2} \pm 4.19 \times 10^{-3}$	$1.14 \times 10^{-5} \pm 1.28 \times 10^{-5}$
	u	$1.88 \times 10^{-2} \pm 1.44 \times 10^{-2}$	$4.32 \times 10^{-4} \pm 1.61 \times 10^{-4}$
2-D heat	u	$1.06 \times 10^{-3} \pm 1.55 \times 10^{-4}$	$1.35 \times 10^{-4} \pm 1.64 \times 10^{-4}$
	u	$4.24 \times 10^{-3} \pm 4.93 \times 10^{-3}$	$4.30 \times 10^{-4} \pm 2.38 \times 10^{-4}$
3-D heat	u	$1.19 \times 10^{-1} \pm 3.61 \times 10^{-3}$	$4.21 \times 10^{-3} \pm 9.79 \times 10^{-4}$
			$1.97 \times 10^{-2} \pm 6.20 \times 10^{-3}$
			$4.70 \times 10^{-2} \pm 5.44 \times 10^{-3}$

Table 2: Comparison of the relative errors for the non-linear equations

equation	PINN	SINN (SI)
1-D Burgers	u	$5.17 \times 10^{-4} \pm 1.50 \times 10^{-4}$
2-D NS_TG	u	$1.62 \times 10^{-4} \pm 4.70 \times 10^{-5}$
	v	$6.97 \times 10^{-4} \pm 2.61 \times 10^{-5}$
2-D NS_random	u	$6.74 \times 10^{-4} \pm 3.26 \times 10^{-4}$
	v	$5.63 \times 10^{-4} \pm 1.99 \times 10^{-4}$
		$5.13 \times 10^{-4} \pm 1.71 \times 10^{-4}$
		$2.20 \times 10^{-3} \pm 7.78 \times 10^{-4}$
		$1.30 \times 10^{-3} \pm 6.66 \times 10^{-5}$
		$2.06 \times 10^{-2} \pm 8.58 \times 10^{-3}$
		$1.53 \times 10^{-2} \pm 6.82 \times 10^{-4}$

4.1 Different order of derivatives

To compare the efficiency between our SINNs and PINNs, we consider a specific one-dimensional (1-D) hyper-diffusion equation with different order of derivatives:

$$\frac{\partial u}{\partial t} - \epsilon \frac{\partial^p u}{\partial x^p} = 0, \quad x \in [0, 2\pi], t \in [0, T],$$

$$u(0, x) = \sum_{k=0}^{N-1} \sin(kx),$$
(24)

where p is the order of the spacial derivatives. To balance the solution of different order, we set $\epsilon = 0.2^p, T = 0.1$ in our experiments. The results are shown in Fig. 1 and Table 3.

Training time One may argue that in Table 3, for the most general derivative term $p = 2$, PINNs are more efficient than SINNs. It is because SINNs have the imaginary part thus the output channels are double the output channels of PINNs. However, we have a more comprehensive comparison in Appendix F, and the conclusion is: if the spacial derivative terms are more than one second-order derivative, including one third-order derivative, or one second-order derivative plus one first-order derivative, our SINNs are more efficient than PINNs; otherwise, PINNs are more efficient.

4.2 Different spectral structures

To verify the approximation of SINNs is not only for the low-frequency solutions, experiments on the diffusion equation (Eq. (25)) are implemented with different N :

$$u_t + au_x - \epsilon u_{xx} = 0, \quad x \in [0, 2\pi], t \in [0, T],$$

$$u(0, x) = \sum_{k=0}^{N-1} \sin(kx).$$
(25)

Table 3: Comparison of the experiments for Eq. (24) with different order. '-' means we can't obtain the value because of the limitations of training time.

	p	Relative error	Training time (hours)	Memory allocated (GB)
PINN	2	$7.35 \times 10^{-2} \pm 7.07 \times 10^{-4}$	0.17	1.18
	4	$1.10 \times 10^{-2} \pm 7.30 \times 10^{-3}$	0.5	2.81
	6	$2.16 \times 10^{-2} \pm 1.75 \times 10^{-3}$	4.39	9.06
	8	-	>30000	26.65
	10	-	-	76.71
SINN (SI)	2	$2.06 \times 10^{-3} \pm 1.51 \times 10^{-3}$	0.33	1.1948
	4	$1.67 \times 10^{-3} \pm 3.25 \times 10^{-4}$	0.33	1.1948
	6	$1.23 \times 10^{-2} \pm 1.36 \times 10^{-3}$	0.33	1.1948
	8	$8.33 \times 10^{-3} \pm 1.91 \times 10^{-4}$	0.33	1.1948
	10	$5.40 \times 10^{-3} \pm 2.33 \times 10^{-4}$	0.35	1.1948
SINN (WL)	2	$8.47 \times 10^{-4} \pm 3.29 \times 10^{-4}$	0.36	1.1968
	4	$1.25 \times 10^{-2} \pm 7.79 \times 10^{-3}$	0.36	1.1968
	6	$1.41 \times 10^{-2} \pm 1.30 \times 10^{-3}$	0.35	1.1968
	8	$8.39 \times 10^{-3} \pm 2.87 \times 10^{-4}$	0.36	1.1968
	10	$5.48 \times 10^{-3} \pm 1.55 \times 10^{-4}$	0.36	1.1968

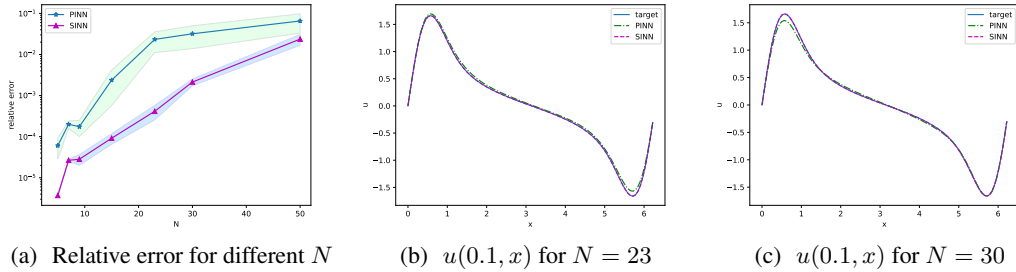


Figure 3: In experiments for the diffusion equation Eq. (25) with different N in $u(0.1, x)$, the relative error with N is plotted in (a). And the solutions of $u(0.1, x)$ for $N = 23$ and 30 are shown in (b) and (c), respectively. Those results indicate that SINNs are robust even with complex spectral structure.

Compared to PINNs, Fig. 3 indicates SINNs are more robust even with a more complex structure in spectral domain. More details including the results of WL for the diffusion equation with different N are presented in Table 6.

4.3 Ablation study of the SI and WL

SI and WL are different approaches designed for the same object, in this section, we provide an ablation study of how to choose the strategies of SI and WL, and how to set the corresponding hyperparameters. To tune the hyperparameters, one should consider the distribution of the Fourier coefficients: the coefficients concentrate more on the low-frequency, and you should have larger ϵ for WL or smaller α and smaller β . To select the approach, ideally, WL is better because this approach can learn all coefficients fully. However, as the relationship between the capability of networks and the complexity of PDEs is unknown, using WL requires additional consideration of the size of the network. If some low-frequencies are out of the capability, WL makes the network continue focusing on them because the hard constraint on the loss function makes the rest frequencies be multiplied by a small weight. So in practice, SI performs better thanks to its soft constraint on the structure of SINNs. We did a series experiments on diffusion equation to show the influence of hyperparameters. The results are depicted in Figs. 4(a) and 4(b) and the details can be found in Appendix G.

Additionally, although we think SI and WL have the same effect, thus using both of them isn't cost-effective, we did extra experiments that combine SI and WL strategies together to verify how SI and WL influence each other. We plot a snapshot of $\epsilon = 10^{-5}$ in Fig. 4(c) which including the

optimal hyperparameters. The experiments shows that combining SI and WL is not an efficient way and sometimes slightly damages the accuracy.

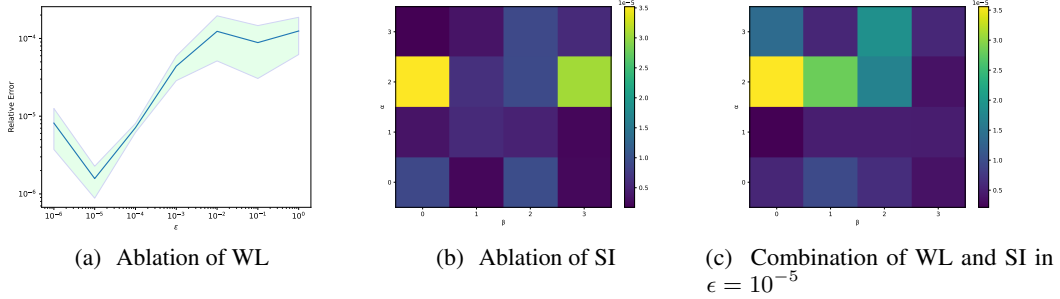


Figure 4: Ablation study in diffusion equation. In Fig. 4(a), the best hyperparameter is $\epsilon = 10^{-5}$, and the corresponding error is $1.58 \times 10^{-6} \pm 6.94 \times 10^{-7}$; in Fig. 4(b), the best hyperparameter for SI is $\alpha = 3, \beta = 0$, and the corresponding error is $1.73 \times 10^{-6} \pm 1.41 \times 10^{-6}$; in Fig. 4(c), the best hyperparameter is $\alpha = 1, \beta = 0, \epsilon = 10^{-5}$, and the corresponding error is $2.14 \times 10^{-6} \pm \times 10^{-7}$.

5 Conclusion and future work

In this study, the Spectral-Informed Neural Networks (SINNs) are developed to approximate the function in the spectral domain. We point out that the difference in learning between the physical domain and the spectral domain is the importance of input points, and therefore specific training strategies are introduced. The chosen Fourier basis helps us compute the spatial derivatives as well as train the neural network efficiently and with low memory allocation. Besides, SINNs have more accurate predictions due to the exponential accuracy of the spectral method. To provide evidence that SINNs have not only a notable reduction in training time but also significant improvements in accuracy, we did a series of experiments on linear and non-linear PDEs.

Limitations The current SINNs also inherit the disadvantages of spectral methods, for some PDEs with complex geometries or detailed boundaries in more than one space variable would cause spectral methods to collapse, and so would SINNs. On the other hand, functions are often more complex in the spectral domain than in the physical domain, thus those functions that cannot be approximated by PINNs always cannot be approximated by SINNs with the same architecture. As for non-linear equations, in our experiments, SINNs are usually unstable when dealing with the aliasing error, due to the nonnegligible bias between Eq. (13) and the ideal loss that the aliasing error is zero.

Future Apart from the positive results shown in this paper, the above limitations remain to be investigated further in the future. For the inherited disadvantages from spectral methods, in essence, the spectral method is a specific type of collocation methods that rely on selected basis functions satisfying boundary conditions. Similar to the spectral methods, the collocation methods ensure the residual of the target equation approaches zero at the collocation points associated with the basis functions. Therefore, the SINNs could be developed based on the valuable insights of earlier studies [22] on collocation methods. To improve the learning capability of SINNs, we can replace the MLP with the architecture from Neural Operators, such as PINO [33] and physics-informed DeepOnets [34]. With the direct derivatives on the spacial, approximating in the spectral domain can make Neural Operators more flexible in dealing with the physics-informed loss. As for the nonnegligible bias, with the bias decreases with the number of grids increases, fine enough grids can make the bias negligible.

Furthermore, during conducting our experiments, we found that SINNs are more sensitive to the initial conditions, so assigning weights [35, 36, 37] in $\tilde{\mathcal{L}}_r$ and $\tilde{\mathcal{L}}_{ic}$ may have a dramatic improvement on SINNs. Some tricks in classical spectral methods can be investigated, for example 1) we can investigate implementing Compressive Sampling [38, 39] on SINNs to further reduce the training time; 2) we can investigate the smoothed series $S_N[u](t, x) = \sum_{k=-N/2}^{N/2-1} \sigma_k \hat{u}(t, k) e^{ikx}$ to handle PDEs with discontinuous solutions or sharp transitions.

References

- [1] M. Raissi, P. Perdikaris, and G. E. Karniadakis, “Physics-informed neural networks: A deep learning framework for solving forward and inverse problems involving nonlinear partial differential equations,” *Journal of Computational physics*, vol. 378, pp. 686–707, 2019.
- [2] B. Yu *et al.*, “The deep Ritz method: a deep learning-based numerical algorithm for solving variational problems,” *Communications in Mathematics and Statistics*, vol. 6, no. 1, pp. 1–12, 2018.
- [3] S. Wojtowytsch and E. Weinan, “Can shallow neural networks beat the curse of dimensionality? a mean field training perspective,” *IEEE Transactions on Artificial Intelligence*, vol. 1, no. 2, pp. 121–129, 2020.
- [4] J. Han, A. Jentzen, and W. E., “Solving high-dimensional partial differential equations using deep learning,” *Proceedings of the National Academy of Sciences*, vol. 115, no. 34, pp. 8505–8510, 2018.
- [5] R. Y. Rubinstein and D. P. Kroese, *Simulation and the Monte Carlo method*. John Wiley & Sons, 2016.
- [6] A. G. Baydin, B. A. Pearlmutter, A. A. Radul, and J. M. Siskind, “Automatic differentiation in machine learning: a survey,” *Journal of machine learning research*, vol. 18, no. 153, pp. 1–43, 2018.
- [7] K. Hornik, “Approximation capabilities of multilayer feedforward networks,” *Neural networks*, vol. 4, no. 2, pp. 251–257, 1991.
- [8] G. E. Karniadakis, I. G. Kevrekidis, L. Lu, P. Perdikaris, S. Wang, and L. Yang, “Physics-informed machine learning,” *Nature Reviews Physics*, vol. 3, no. 6, pp. 422–440, 2021.
- [9] L. Yang, X. Meng, and G. E. Karniadakis, “B-PINNs: Bayesian physics-informed neural networks for forward and inverse PDE problems with noisy data,” *Journal of Computational Physics*, vol. 425, p. 109913, 2021.
- [10] P. Ren, C. Rao, Y. Liu, J.-X. Wang, and H. Sun, “PhyCRNet: Physics-informed convolutional-recurrent network for solving spatiotemporal PDEs,” *Computer Methods in Applied Mechanics and Engineering*, vol. 389, p. 114399, 2022.
- [11] L. Sliwinski and G. Rigas, “Mean flow reconstruction of unsteady flows using physics-informed neural networks,” *Data-Centric Engineering*, vol. 4, p. e4, 2023.
- [12] X. Jin, S. Cai, H. Li, and G. E. Karniadakis, “NSFnets (Navier-Stokes flow nets): Physics-informed neural networks for the incompressible Navier-Stokes equations,” *Journal of Computational Physics*, vol. 426, p. 109951, 2021.
- [13] Z. Mao, A. D. Jagtap, and G. E. Karniadakis, “Physics-informed neural networks for high-speed flows,” *Computer Methods in Applied Mechanics and Engineering*, vol. 360, p. 112789, 2020.
- [14] Z. Fang and J. Zhan, “A physics-informed neural network framework for PDEs on 3D surfaces: Time independent problems,” *IEEE Access*, vol. 8, pp. 26328–26335, 2019.
- [15] G. S. Misyris, A. Venzke, and S. Chatzivasileiadis, “Physics-informed neural networks for power systems,” in *2020 IEEE power & energy society general meeting (PESGM)*, pp. 1–5, IEEE, 2020.
- [16] H. Gao, L. Sun, and J.-X. Wang, “PhyGeoNet: Physics-informed geometry-adaptive convolutional neural networks for solving parameterized steady-state PDEs on irregular domain,” *Journal of Computational Physics*, vol. 428, p. 110079, 2021.
- [17] C. Rao, P. Ren, Q. Wang, O. Buyukozturk, H. Sun, and Y. Liu, “Encoding physics to learn reaction–diffusion processes,” *Nature Machine Intelligence*, vol. 5, no. 7, pp. 765–779, 2023.
- [18] R. Sharma and V. Shankar, “Accelerated training of physics-informed neural networks (pinns) using meshless discretizations,” *Advances in Neural Information Processing Systems*, vol. 35, pp. 1034–1046, 2022.
- [19] M. Xia, L. Böttcher, and T. Chou, “Spectrally adapted physics-informed neural networks for solving unbounded domain problems,” *Machine Learning: Science and Technology*, vol. 4, no. 2, p. 025024, 2023.

- [20] B. Lütjens, C. H. Crawford, M. Veillette, and D. Newman, “Spectral pinns: Fast uncertainty propagation with physics-informed neural networks,” in *The Symbiosis of Deep Learning and Differential Equations*, 2021.
- [21] A. Griewank and A. Walther, *Evaluating derivatives: principles and techniques of algorithmic differentiation*. SIAM, 2008.
- [22] C. Canuto, M. Y. Hussaini, A. Quarteroni, and T. A. Zang, *Spectral Methods in Fluid Dynamics*. Scientific Computation, Heidelberg: Springer Berlin, 1 ed., 1988.
- [23] S. A. Orszag, “Numerical simulation of incompressible flows within simple boundaries: accuracy,” *Journal of Fluid Mechanics*, vol. 49, no. 1, pp. 75–112, 1971.
- [24] J. Bettencourt, M. J. Johnson, and D. Duvenaud, “Taylor-mode automatic differentiation for higher-order derivatives in JAX,” in *Program Transformations for ML Workshop at NeurIPS 2019*, 2019.
- [25] S. Tan, *Higher-Order Automatic Differentiation and Its Applications*. PhD thesis, Massachusetts Institute of Technology, 2023.
- [26] K. Tang, X. Wan, and C. Yang, “DAS-PINNs: A deep adaptive sampling method for solving high-dimensional partial differential equations,” *Journal of Computational Physics*, vol. 476, p. 111868, 2023.
- [27] C. Wu, M. Zhu, Q. Tan, Y. Kartha, and L. Lu, “A comprehensive study of non-adaptive and residual-based adaptive sampling for physics-informed neural networks,” *Computer Methods in Applied Mechanics and Engineering*, vol. 403, p. 115671, 2023.
- [28] L. Lu, X. Meng, Z. Mao, and G. E. Karniadakis, “DeepXDE: A deep learning library for solving differential equations,” *SIAM review*, vol. 63, no. 1, pp. 208–228, 2021.
- [29] R. H. Kraichnan, “Inertial ranges in two-dimensional turbulence,” *The Physics of Fluids*, vol. 10, no. 7, pp. 1417–1423, 1967.
- [30] Z. Li, N. Kovachki, K. Azizzadenesheli, B. Liu, K. Bhattacharya, A. Stuart, and A. Anandkumar, “Fourier neural operator for parametric partial differential equations,” 2020.
- [31] S. Wang, S. Sankaran, and P. Perdikaris, “Respecting causality is all you need for training physics-informed neural networks,” *arXiv preprint arXiv:2203.07404*, 2022.
- [32] A. Quarteroni, R. Sacco, and F. Saleri, *Numerical mathematics*, vol. 37. Springer Science & Business Media, 2006.
- [33] Z. Li, H. Zheng, N. Kovachki, D. Jin, H. Chen, B. Liu, K. Azizzadenesheli, and A. Anandkumar, “Physics-informed neural operator for learning partial differential equations,” *ACM/JMS Journal of Data Science*, 2021.
- [34] S. Wang, H. Wang, and P. Perdikaris, “Learning the solution operator of parametric partial differential equations with physics-informed DeepOnets,” *Science advances*, vol. 7, no. 40, p. eabi8605, 2021.
- [35] S. Wang, X. Yu, and P. Perdikaris, “When and why PINNs fail to train: A neural tangent kernel perspective,” *Journal of Computational Physics*, vol. 449, p. 110768, 2022.
- [36] L. D. McClenny and U. M. Braga-Neto, “Self-adaptive physics-informed neural networks,” *Journal of Computational Physics*, vol. 474, p. 111722, 2023.
- [37] S. J. Anagnostopoulos, J. D. Toscano, N. Stergiopoulos, and G. E. Karniadakis, “Learning in PINNs: Phase transition, total diffusion, and generalization,” *arXiv preprint arXiv:2403.18494*, 2024.
- [38] E. J. Candès *et al.*, “Compressive sampling,” in *Proceedings of the international congress of mathematicians*, vol. 3, pp. 1433–1452, Madrid, Spain, 2006.
- [39] C. Bayındır, “Compressive spectral method for the simulation of the nonlinear gravity waves,” *Scientific reports*, vol. 6, no. 1, p. 22100, 2016.
- [40] J. F. Lucas, *Introduction to abstract mathematics*. Rowman & Littlefield, 1990.
- [41] S. A. Orszag, “On the elimination of aliasing in finite-difference schemes by filtering high-wavenumber components,” *Journal of Atmospheric Sciences*, vol. 28, no. 6, pp. 1074–1074, 1971.

- [42] T. Y. Hou and R. Li, “Computing nearly singular solutions using pseudo-spectral methods,” *Journal of Computational Physics*, vol. 226, no. 1, pp. 379–397, 2007.
- [43] D. P. Kingma and J. Ba, “Adam: A method for stochastic optimization,” *arXiv preprint arXiv:1412.6980*, 2014.
- [44] S. Gottlieb and C.-W. Shu, “Total variation diminishing Runge-Kutta schemes,” *Math. Comput.*, vol. 67, pp. 73–85, 1998.

A Faà di Bruno’s formula

Given f, g are sufficiently smooth functions, Faà di Bruno’s formula states that the n -th derivative of $f(g(x))$ is a sum of products of various orders of derivatives of the component functions:

$$\frac{d^n}{dx^n} f(g(x)) = (f \circ g)^{(n)}(x) = \sum_{\pi \in \Pi} f^{(|\pi|)}(g(x)) \cdot \prod_{B \in \pi} g^{(|B|)}(x),$$

where Π is the set of all partitions of the set $\{1, \dots, n\}$, $|\pi|$ is the number of blocks in the partition π , and $|B|$ is the number of elements in the block B . Since Faà di Bruno’s formula is a generalization of the chain rule used in first-order, one can directly apply this formula to achieve accurate higher-order AD efficiently by avoiding a lot of redundant computations. However, the total number of partitions of an n -element set is the Bell number [40]: $\#\{\Pi\} = B_n = \sum_{k=0}^n \binom{n}{k} B_k$ that increases exponentially with the order n (Fig. 5).

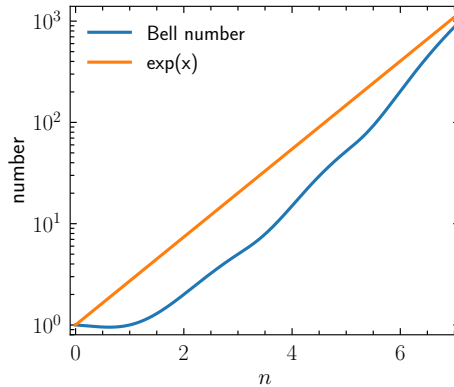


Figure 5: Comparison of the total number between the Bell number and the exponential function.

B Aliasing error

The quadratic non-linear term $w(x) = u(x)v(x)$ can be regarded as the convolution sum of the Fourier expansions of the corresponding two terms in spectral methods, *i.e.*,

$$\hat{w}(k) = \sum_{m+n=k} \hat{u}(m)\hat{v}(n), \quad (26)$$

where \hat{w} , \hat{u} , and \hat{v} represent the Fourier coefficients of $u(x)$, $v(x)$, and $w(x)$, respectively. In practical computations, when dealing with truncated Fourier series consisting of only N components, a challenge arises: some frequencies of the summation of the two terms exceed the range of the truncated frequency. This issue stems from the periodic nature of the discrete Fourier transform, where components outside the frequency range are mapped back into the range as lower or higher frequency components, leading to aliasing errors in the nonlinear terms. For instance, components whose frequencies satisfy $m + n > N/2 - 1$ are erroneously identified as components of frequency $(m + n - N)$. Two truncation methods, the 2/3 rule [41] and the Fourier smoothing method [42], are designed to retain the components within the range of $-N/3$ to $N/3 - 1$ for the nonlinear terms. The 2/3 rule sets the last 1/3 of the high-frequency modes to zero, leaving the rest unchanged,

while the Fourier smoothing method uses an exponential function $y = e^{-36(|k|/N)^{36}}$ to filter out the high-frequency modes. The Fourier smoothing method is employed in our SINNs since it can capture more effective Fourier modes and make a more accurate solution [42].

C Details of Experiments

In the following experiments, we proceed by training the model via stochastic gradient descent using the Adam [43] optimizer with the exponential decay learning rate. The hyperparameters for exponential decay are: the initial learning rate is 10^{-3} , the decay rate is 0.95 and the number of transition steps is 10000. The MLP is equipped with the Sigmoid Linear Unit (SiLU) activations and Xavier initialization.

Note that there is no injection of external source terms in our experiments, resulting in a decay of the quantities, including temperature and energy, over time. As time increases, the related functions gradually become smoother, and the overall flow field tends to be constant. Herein, to clearly demonstrate the advantages and performance of our SINNs, the temporal domain is restricted to the interval when the flow field undergoes significant changes. Additionally, we did an experiment in a long temporal domain for the 1-D convection-diffusion equation with periodic boundary conditions.

C.1 The experiments on linear equations

C.1.1 1-D problems

In 1-D problems, we discretize the spatial domain to 100 points and the temporal domain to 100 points, thus the total size of the discretization for PINNs is 100×100 . Thanks to the symmetric of real functions in the spectral domain, the total size of the discretization for SINNs is 51×100 . The MLP we used for both PINNs and SINNs is 10×100 : 10 layers and every hidden layer has 100 neurons. We train both PINNs and SINNs for 5×10^5 iterations.

Convection-diffusion equation (convection-diffusion) Our first experiment is the 1-D convection-diffusion equation with periodic boundary conditions, and the convection-diffusion equation can be expressed as follows:

$$\begin{aligned} u_t + au_x - \epsilon u_{xx} &= 0, x \in [0, 2\pi], t \in [0, T], \\ u(0, x) &= \sum_{k=0}^{N-1} \sin(kx), \end{aligned} \quad (27)$$

with the analytic solution

$$u(t, x) = \sum_{k=0}^{N-1} \sin(kx - kat) e^{-\epsilon k^2 t}, \quad (28)$$

where $T = 0.1$, $\epsilon = 0.01$, $a = 0.1$, and $N = 6$ in our experiments.

Additionally, to verify our methods on long temporal domain, we did two experiments one is $T = 1$ (discretize to 100 points) and another is $T = 10$ (discretize to 1000 points).

Table 4: Long temporal domain of $T = 1$

$t(s)$	0.10	0.30	0.50	0.70	0.90	1.00
relative error	1.43×10^{-5}	1.55×10^{-5}	1.39×10^{-5}	1.44×10^{-5}	1.47×10^{-5}	1.49×10^{-5}

Table 5: Long temporal domain of $T = 10$

$t(s)$	1.00	3.00	5.00	7.00	9.00	10.00
relative error	8.86×10^{-5}	6.48×10^{-5}	6.59×10^{-5}	4.98×10^{-5}	3.96×10^{-5}	4.21×10^{-5}

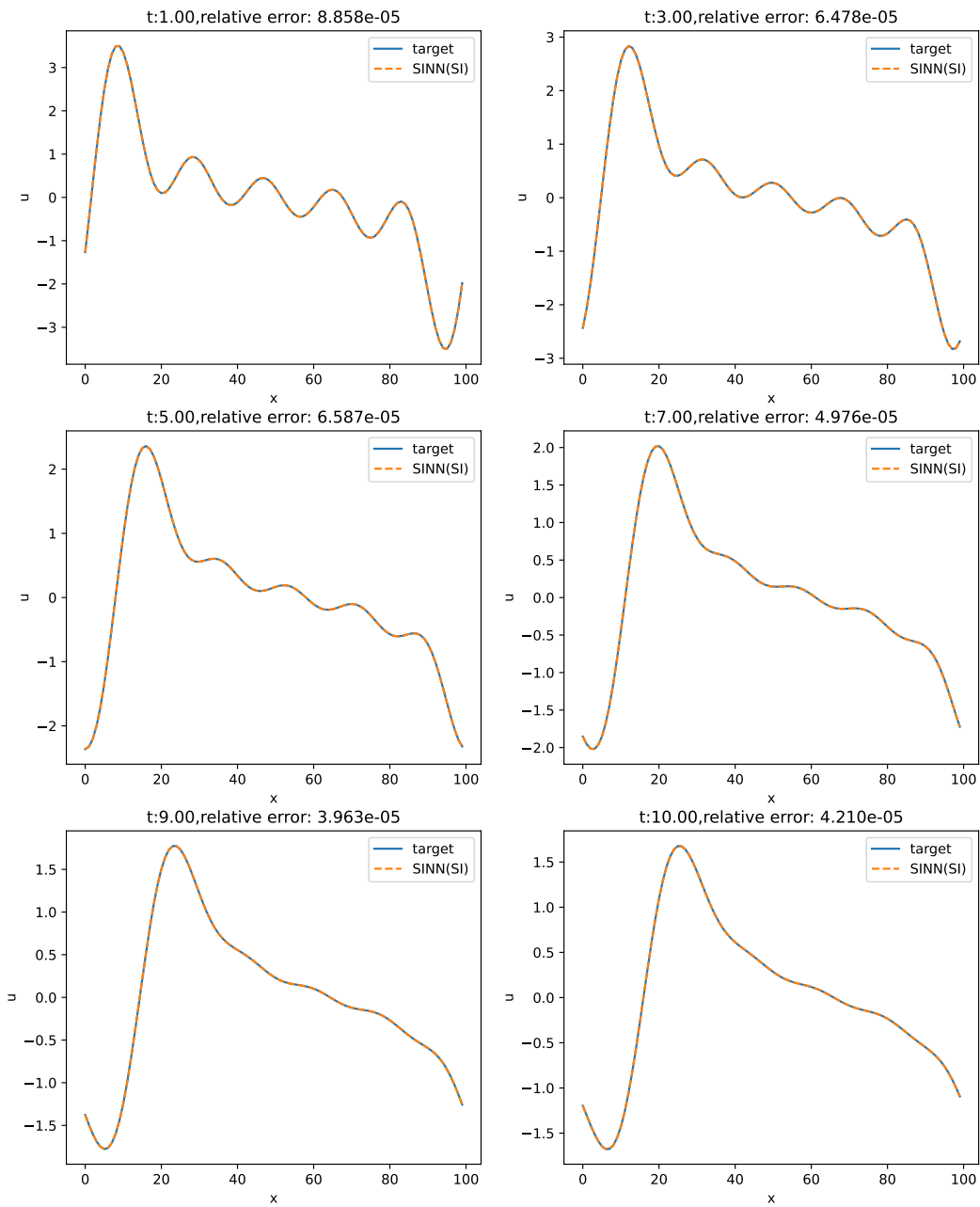


Figure 6: Lone temporal domain experiment of $T = 10$, with the time t increases, the function becomes smoother and the relative error becomes even smaller. Furthermore, the error is consistency on time showing there is no error accumulation on SINNs

Diffusion equation (diffusion) Another set of experiments on 1-D linear equations is about the diffusion equation, which can be written as

$$\begin{aligned} u_t &= \epsilon u_{xx}, \quad x \in [0, 2\pi], \quad t \in [0, T], \\ u(0, x) &= \sum_{k=0}^{N-1} \sin(kx), \end{aligned} \quad (29)$$

with the analytic solution

$$u(t, x) = \sum_{k=0}^{N-1} \sin(kx) e^{-\epsilon k^2 t}, \quad (30)$$

where $T = 0.1$ and $\epsilon = 1.0$ in our experiments. Based on PINNs and SINNs with sampling by importance, Fig. 3 illustrates two groups of experiments with varied N . Besides, Table 1 shows the experimental results with $N = 23$, while Table 6 presents more results with different N .

Table 6: Comparison of the relative errors for the diffusion equation with different N in Eq. (30)

N	PINN	SINN (SI)	SINN (WL)
5	$6.07 \times 10^{-5} \pm 3.17 \times 10^5$	$3.71 \times 10^{-6} \pm 1.59 \times 10^{-7}$	$7.94 \times 10^{-5} \pm 1.80 \times 10^{-5}$
7	$2.00 \times 10^{-4} \pm 4.04 \times 10^5$	$2.66 \times 10^{-5} \pm 1.54 \times 10^{-6}$	$1.46 \times 10^{-4} \pm 5.36 \times 10^{-5}$
9	$1.75 \times 10^{-4} \pm 7.42 \times 10^5$	$2.82 \times 10^{-5} \pm 8.11 \times 10^{-6}$	$6.97 \times 10^{-5} \pm 9.18 \times 10^{-6}$
15	$2.38 \times 10^{-3} \pm 1.80 \times 10^3$	$9.17 \times 10^{-5} \pm 2.62 \times 10^{-5}$	$1.44 \times 10^{-4} \pm 4.27 \times 10^{-5}$
23	$2.33 \times 10^{-2} \pm 1.21 \times 10^2$	$4.15 \times 10^{-4} \pm 1.58 \times 10^{-4}$	$4.30 \times 10^{-4} \pm 2.38 \times 10^{-4}$
30	$3.19 \times 10^{-2} \pm 1.80 \times 10^2$	$2.13 \times 10^{-3} \pm 3.91 \times 10^{-4}$	$5.40 \times 10^{-1} \pm 3.00 \times 10^{-1}$
50	$6.55 \times 10^{-2} \pm 3.22 \times 10^2$	$2.37 \times 10^{-2} \pm 6.89 \times 10^{-3}$	$7.59 \times 10^{-1} \pm 2.28 \times 10^{-1}$

One may observe that the weighted loss method fails when $N > 30$. Because the weighted loss forces SINNs to pay more attention on the low-frequency part, SINNs with weighted loss will abandon the high-frequency if the loss on low-frequency is not small enough.

C.1.2 2-D problems

In 2-D problems, the MLP we used for both PINNs and SINNs is 10×100 : 10 layers and every hidden layer has 100 neurons. We train both PINNs and SINNs for 10^6 iterations.

Heat equation with analytic solution (heat_analytic) For a 2-D linear problem, the heat equation with the following initial condition is considered here:

$$\begin{aligned} u_t &= \epsilon (u_{xx} + u_{yy}), \quad \mathbf{x} \in [0, 2\pi]^2, \quad t \in [0, T], \\ u(0, \mathbf{x}) &= \sum_{k=0}^{N-1} [\sin(kx) + \sin(ky)], \end{aligned} \quad (31)$$

with the analytic solution

$$u(t, \mathbf{x}) = \sum_{k=0}^{N-1} [\sin(kx) + \sin(ky)] e^{-\epsilon k^2 t}, \quad (32)$$

where $T = 0.01$, $\epsilon = 1.0$, and $N = 10$ in our experiment. The discretization of the spatial and temporal domains is set to 100×100 and 10 points, respectively. Thus, the total size of the discretization for PINNs is $100 \times 100 \times 10$, while the total size for SINNs can be reduced to $51 \times 100 \times 10$ due to the Fourier transform for real functions.

Heat equation with random initialization (heat_random) The 2-D heat equation with the Gaussian random initial condition is included here, which can be written as

$$\begin{aligned}
u_t &= \epsilon (u_{xx} + u_{yy}), \quad \mathbf{x} \in [0, 2\pi]^2, t \in [0, T], \\
\hat{u}(0, \mathbf{k}) &= \hat{g}(\mathbf{k}), \\
\hat{g}(\mathbf{k}) &= \begin{cases} 10^4 \sqrt{0.123456/H(1)} h(\mathbf{k}), & \frac{1}{2} \leq |\mathbf{k}| < \frac{3}{2}, \\ 10^4 \sqrt{0.654321/H(2)} h(\mathbf{k}), & \frac{3}{2} \leq |\mathbf{k}| < \frac{5}{2}, \\ 10^4 \sqrt{0.345612/H(3)} h(\mathbf{k}), & \frac{5}{2} \leq |\mathbf{k}| < \frac{7}{2}, \\ 10^4 \sqrt{0.216543/H(4)} h(\mathbf{k}), & \frac{7}{2} \leq |\mathbf{k}| < \frac{9}{2}, \\ 10^4 \sqrt{0.561234/H(5)} h(\mathbf{k}), & \frac{9}{2} \leq |\mathbf{k}| < \frac{11}{2}, \\ 10^4 \sqrt{0.432165/H(6)} h(\mathbf{k}), & \frac{11}{2} \leq |\mathbf{k}| < \frac{13}{2}, \\ 0, & |\mathbf{k}| \geq \frac{13}{2}, \end{cases} \quad (33) \\
H(n) &= \sum_{n-\frac{1}{2} \leq |\mathbf{k}| < n+\frac{1}{2}} |h(\mathbf{k})|^2,
\end{aligned}$$

where $h \in \mathbb{C}$ generated by standard normal distribution fulfills the symmetry $h(\mathbf{k}) = \bar{h}(-\mathbf{k})$, and the parameters $T = 0.01$, $\epsilon = 1.0$, and $N = 10$ are taken in our experiment. The spatial and temporal domains are discretized to 100×100 and 6 points, respectively. The total size of the discretization for PINNs is $100 \times 100 \times 6$, while the total size for SINNs is reduced to $51 \times 100 \times 6$ since the functions are real. The solutions $u(0.01, \mathbf{x})$ in our experiments for the 2-D heat equation with the Gaussian random initial condition are plotted in Fig. 7. The spectral method in Appendix H computes the numerical solution $u(0.01, \mathbf{x})$ with a sufficiently small time step.

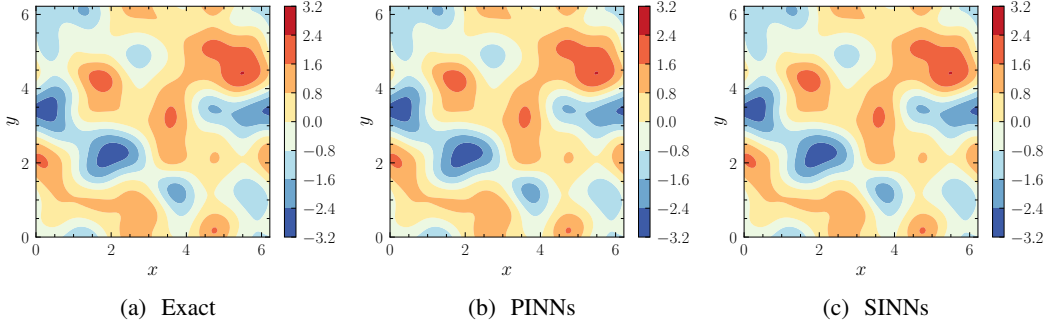


Figure 7: The exact solution, the predicted solution by PINNs, and the predicted solution by SINNs for $u(0.01, \mathbf{x})$ in the 2-D heat equation with the Gaussian random initial condition are displayed in (a), (b), and (c), respectively.

C.1.3 3-D problems

Heat equation with analytic solution (heat_analytic) To compare SINNs and PINNs for 3-D linear equations, a heat equation problem is considered here, which has the form

$$\begin{aligned}
u_t &= \epsilon (u_{xx} + u_{yy} + u_{zz}), \quad \mathbf{x} \in [0, 2\pi]^3, t \in [0, T], \\
u(0, \mathbf{x}) &= \sum_{k=0}^{N-1} [\sin(kx) + \sin(ky) + \sin(kz)], \quad (34)
\end{aligned}$$

with the analytic solution

$$u(t, \mathbf{x}) = \sum_{k=0}^{N-1} [\sin(kx) + \sin(ky) + \sin(kz)] e^{-\epsilon k^3 t}. \quad (35)$$

where $T = 0.01$, $\epsilon = 1.0$, and $N = 5$ in our experiment. The discretized spatial and temporal domains are $100 \times 100 \times 100$ and 10 points, respectively. The total size of the discretization for PINNs is $100 \times 100 \times 100 \times 10$, while the total size for SINNs is decreased to $51 \times 100 \times 100 \times 10$ for the real function u .

C.2 The experiments on non-linear equations

C.2.1 1-D problems

Burgers equation (Burgers) One of the most important 1-D nonlinear equations is the Burgers equation, taking the following form:

$$\begin{aligned} u_t &= \nu u_{xx} - uu_x, \quad x \in [0, 2\pi], t \in [0, T], \\ u(0, x) &= \sum_{k=1}^N \sin(kx) \end{aligned} \quad (36)$$

where $T = 0.1$, $N = 3$ and $\nu = \pi/150$ in our experiment. The discretization of the spatial and temporal domains is set to 100 and 11 points, respectively. The total size of the discretization for PINNs is 100×11 , while the total size for SINNs is 51×11 for a real u .

C.2.2 2-D problems

NS equations with Taylor–Green vortex (NS_TG) The 2-D nonlinear NS equation is the same as Eq. (11) with $T = 2$, $\nu = 2\pi/100$, and $\mathbf{g}(\mathbf{x}) = (-\cos(x)\sin(y), \sin(x)\cos(y))$ in our experiment. The spatial and temporal domains are discretized to 100×100 and 11 points, respectively. The total size for PINNs is $100 \times 100 \times 11$, while the total size for SINNs is $51 \times 100 \times 11$ since \mathbf{u} is real.

NS equations with random initialization (NS_random) The 2-D NS equation Eq. (11) is also included here with $T = 2$, $\nu = 2\pi/100$, and a random initial condition $\mathbf{g}(\mathbf{x})$, namely,

$$\begin{aligned} \hat{\mathbf{u}}(0, \mathbf{k}) &= \hat{\mathbf{g}}(\mathbf{k}), \\ \hat{\mathbf{g}}(\mathbf{k}) &= \begin{cases} 10^4 \sqrt{0.123456/H(1)} (\mathbf{h} - \mathbf{k}\mathbf{k} \cdot \mathbf{h}/|\mathbf{k}|^2), & \frac{1}{2} \leq |\mathbf{k}| < \frac{3}{2}, \\ 10^4 \sqrt{0.654321/H(2)} (\mathbf{h} - \mathbf{k}\mathbf{k} \cdot \mathbf{h}/|\mathbf{k}|^2), & \frac{3}{2} \leq |\mathbf{k}| < \frac{5}{2}, \\ 10^4 \sqrt{0.345612/H(3)} (\mathbf{h} - \mathbf{k}\mathbf{k} \cdot \mathbf{h}/|\mathbf{k}|^2), & \frac{5}{2} \leq |\mathbf{k}| < \frac{7}{2}, \\ \mathbf{0}, & |\mathbf{k}| \geq \frac{7}{2}, \end{cases} \quad (37) \\ H(n) &= \sum_{n-\frac{1}{2} \leq |\mathbf{k}| < n+\frac{1}{2}} |\mathbf{h}(\mathbf{k})|^2, \end{aligned}$$

where $\mathbf{h} \in \mathbb{C}$ generated by standard normal distribution fulfills the symmetry $\mathbf{h}(\mathbf{k}) = \bar{\mathbf{h}}(-\mathbf{k})$. The spatial and temporal domains are discretized to 100×100 and 11 points, respectively. And the total size for PINNs is $100 \times 100 \times 11$, while the total size for SINNs is reduced to $51 \times 100 \times 11$ for a real \mathbf{u} . The predicted solutions from the SINNs for this problem, including the x -component u and y -component v of the velocity $\mathbf{u}(2, \mathbf{x}) = (u, v)$, are plotted in Fig. 8. And the corresponding numerical solution $\mathbf{u}(2, \mathbf{x})$ is obtained with a sufficiently small time step by the spectral method in Appendix H.

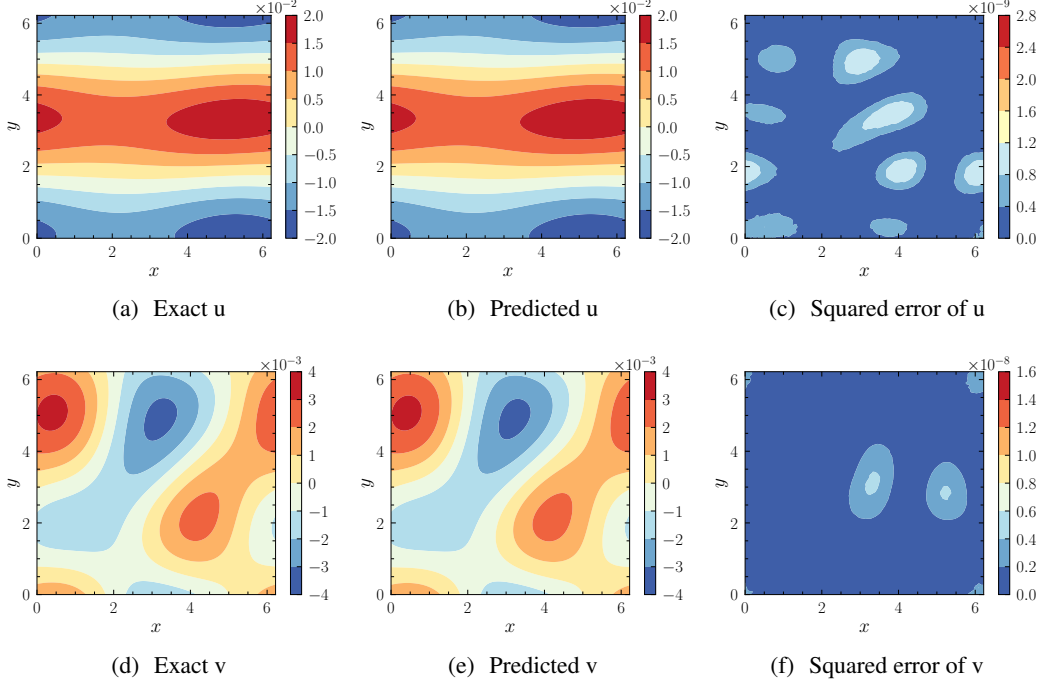


Figure 8: For the 2-D NS equations Eq. (11) with the Gaussian random initial condition, exact solutions of $u(2, \mathbf{x})$ and $v(2, \mathbf{x})$ are plotted on Figs. 8(a) and 8(d) respectively, predicted solutions by SINNs of $u(2, \mathbf{x})$ and $v(2, \mathbf{x})$ are plotted on Figs. 8(b) and 8(e) respectively, and the corresponding squared errors are plotted Figs. 8(c) and 8(f)

C.3 The metrics of the relative error

The metric we use is the relative L2 error as follows:

$$E = \frac{\sqrt{\sum_{i=1}^N |u^\theta(t^i, x^i) - u^T(t^i, x^i)|^2}}{\sqrt{\sum_{i=1}^N |u^T(t^i, x^i)|^2}}, \quad (38)$$

where u^T is the target solution and u^θ is the trained approximation. In cases where u^T cannot be analytically represented, the spectral method in Appendix H is utilized to obtain high-accuracy numerical solutions.

D Some details involved in the spectral form of the incompressible NS equations

This appendix presents the details of the derivation of Eq. (12) and the calculation of non-linear terms \hat{N} in spectral space.

Considering the periodic boundary conditions, by applying the Fourier transform on both sides of Eq. (11), the NS equations in the spectral space are expressed as

$$i\mathbf{k} \cdot \hat{\mathbf{u}} = 0, \quad (39a)$$

$$\partial_t \hat{\mathbf{u}} + \hat{N} = -i\mathbf{k}\hat{p} - \nu|\mathbf{k}|^2 \hat{\mathbf{u}}. \quad (39b)$$

The continuity equation reveals that frequency and velocity are orthogonal in spectral space; by taking the frequency dot product on both sides of the momentum equation Eq. (39b), the relationship between the pressure and the non-linear term can be obtained,

$$\mathbf{k} \cdot \hat{N} = -i|\mathbf{k}|^2 \hat{p}. \quad (40)$$

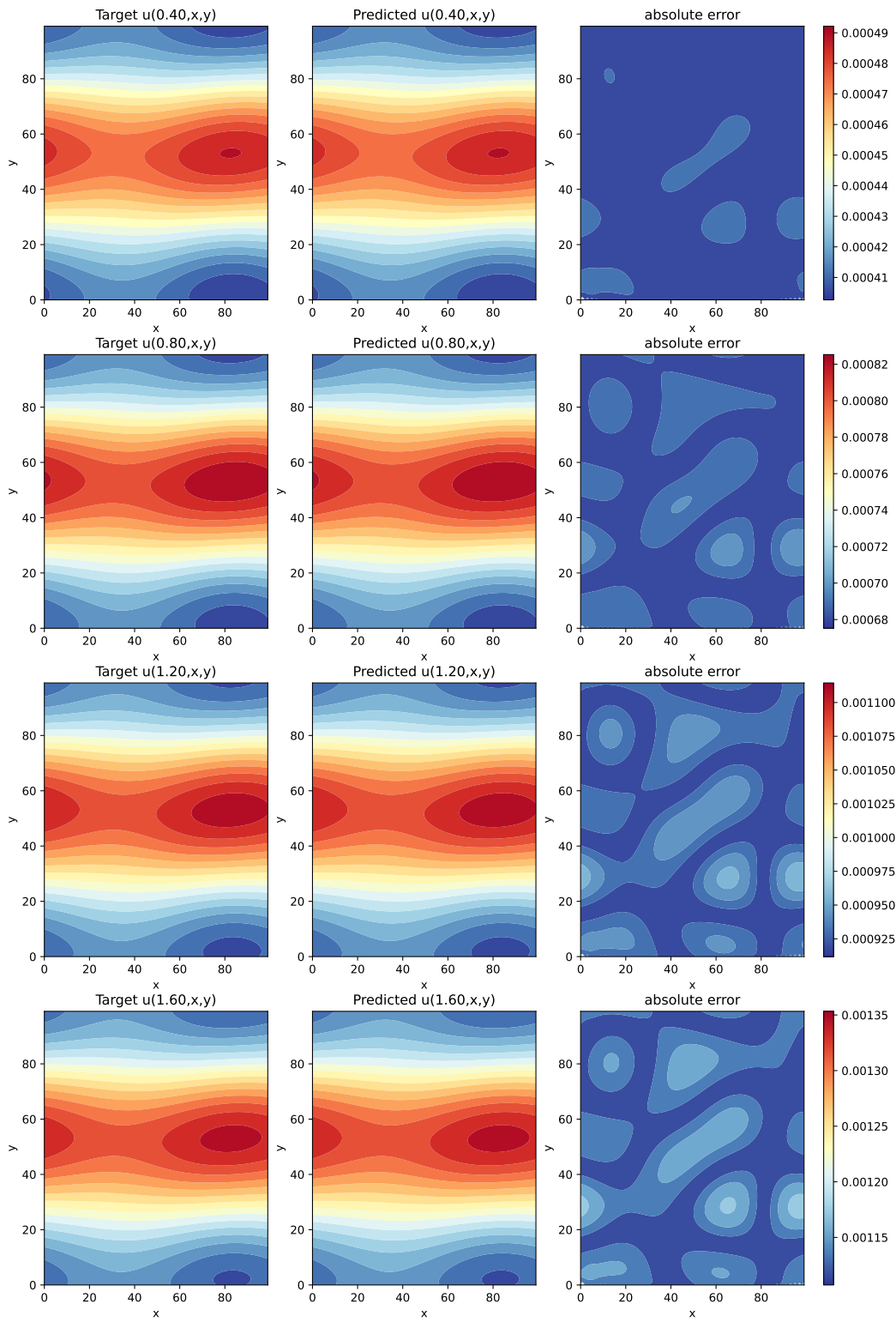


Figure 9: Representative snapshots of the predicted u against the ground truth at $t = 0.4, 0.8, 1.2, 1.6$

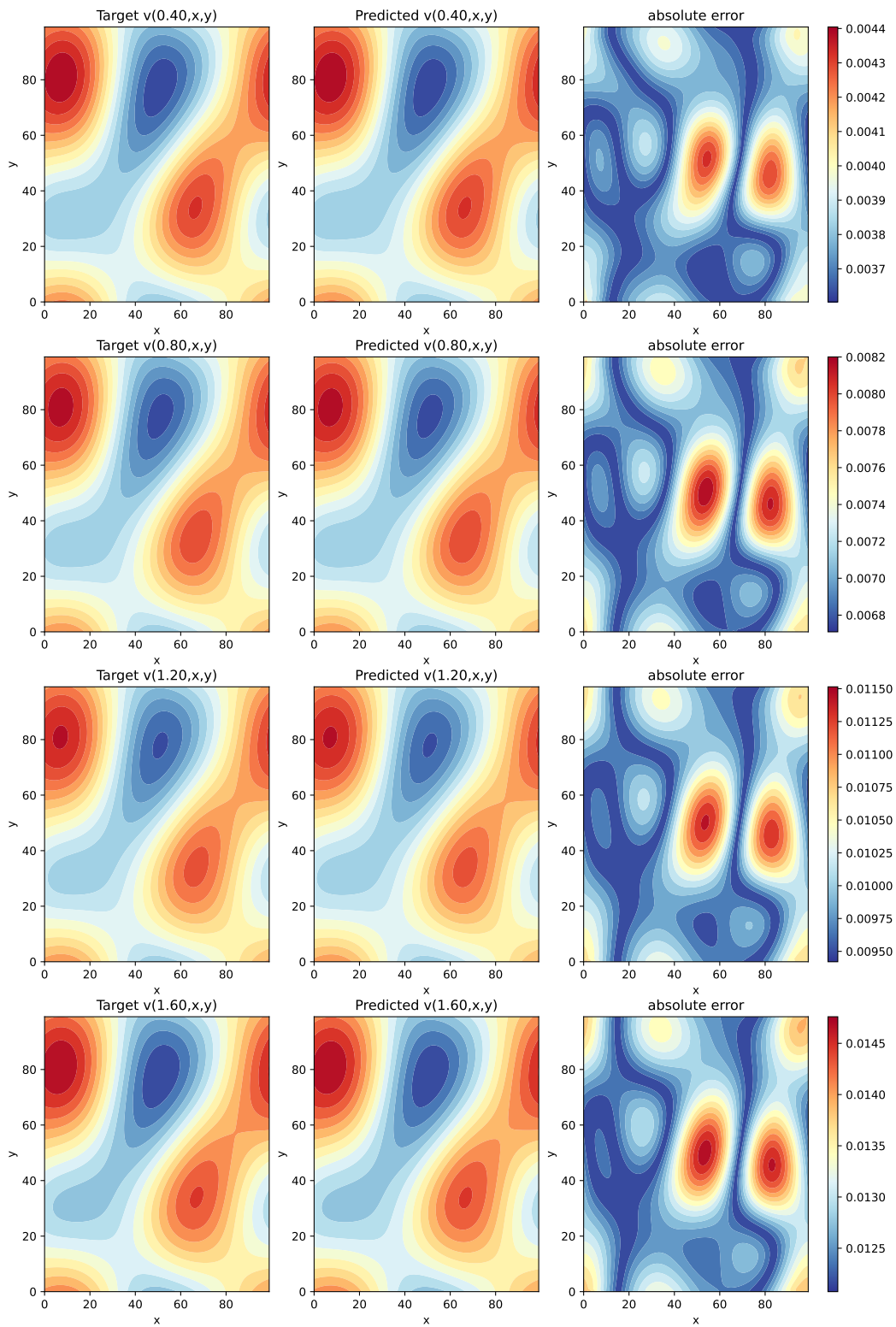


Figure 10: Representative snapshots of the predicted v against the ground truth at $t = 0.4, 0.8, 1.2, 1.6$

Eliminating the pressure in the momentum equation Eq. (39b), the form of Eq. (12b) can be finally obtained.

According to the identities in field theory, the non-linear terms in Eq. (11b) can be expressed in the form

$$\mathbf{N} = \mathbf{u} \cdot \nabla \mathbf{u} = \nabla (\mathbf{u} \cdot \mathbf{u}/2) + (\nabla \times \mathbf{u}) \times \mathbf{u}, \quad (41)$$

where the term $\nabla (\mathbf{u} \cdot \mathbf{u}/2)$ has no contribution to Eq. (12b), and the non-linear term can be simplified as the rotational form [22] $\mathbf{N} = (\nabla \times \mathbf{u}) \times \mathbf{u}$. The specific calculation of non-linear terms in spectral space can be written as

$$\mathbf{N} = \mathcal{D} [\mathcal{F}^{-1} [i\mathbf{k} \times \hat{\mathbf{u}}(t, \mathbf{k})] \times \mathcal{F}^{-1} [\hat{\mathbf{u}}(t, \mathbf{k})]], \quad (42)$$

where \mathcal{D} is the dealiasing operator in Appendix B.

E Simplification of weighted residual loss

Suppose

$$\mathcal{F}_i = \left| \partial_t \hat{u}^\theta(t_r^i, \mathbf{k}^i) + (k_x^i)^2 \hat{u}^\theta(t_r^i, \mathbf{k}^i) + (k_y^i)^2 \hat{u}^\theta(t_r^i, \mathbf{k}^i) \right|^2, \quad (43)$$

and $\mathcal{L}_r = \{\mathcal{F}_i\}_{i=0}^{N_r}$ is the vectorization of \mathcal{F}_i sorted by $\|\mathbf{k}\|_1$, then the Eq. (16) can be simplified to :

$$\tilde{\mathcal{L}}_r(\theta) = \frac{1}{M} (\exp(-\epsilon W \mathcal{L}_r))^T \mathcal{L}_r. \quad (44)$$

where $W = \{w_{ij}\} \in \mathbb{R}^{N_r \times N_r}$ and

$$w_{ij} = \begin{cases} 1 & \text{if } j < \#\{\|\mathbf{k}\|_1 \leq \|\mathbf{k}^i\|_1\}, \\ 0 & \text{otherwise.} \end{cases} \quad (45)$$

Furthermore, we can decompose $W = W^1 W^2 W^3$ where $W^1 = \{w_{ij}^1\} \in \mathbb{R}^{N_r \times (M-1)}$, $W^2 = \{w_{ij}^2\} \in \mathbb{R}^{(M-1) \times (M-1)}$, and $W^3 = \{w_{ij}^3\} \in \mathbb{R}^{(M-1) \times N_r}$. For

$$w_{ij}^1 = \begin{cases} 1 & \text{if } \#\{\|\mathbf{k}\|_1 \leq \|\mathbf{k}^i\|_1\} < j \leq \#\{\|\mathbf{k}\|_1 \leq \|\mathbf{k}^i\|_1 + 1\}, \\ 0 & \text{otherwise.} \end{cases} \quad (46)$$

$$w_{ij}^2 = \begin{cases} 1 & \text{if } j \leq i, \\ 0 & \text{otherwise.} \end{cases} \quad (47)$$

$$w_{ij}^3 = \begin{cases} 1 & \text{if } \#\{\|\mathbf{k}\|_1 < \|\mathbf{k}^j\|_1\} < i \leq \#\{\|\mathbf{k}\|_1 \leq \|\mathbf{k}^j\|_1\}, \\ 0 & \text{otherwise.} \end{cases} \quad (48)$$

F Comparison of training time

Table 7: Comparison of the training time of the linear equations

	equation	PINN	SINN (SI)	SINN (WL)
1-D	convection-diffusion [†]	1.92 h	1.63 h	1.71 h
	diffusion [†]	See Table 3		
2-D	heat [†]	8.67 h	5.28 h	7.68 h
	heat_random [†]	7.87 h	4.78 h	7.01 h
3-D	heat [‡]	20.94 h	14.11 h	15.03 h

Those superscripts are:

†: train on single Tesla V100-SXM2-16GB with CUDA version: 12.3.

‡: train on single NVIDIA A100-SXM4-80GB with CUDA version: 11.2.

Table 8: Comparison of the training time of the non-linear equations

	equation	PINN	SINN
1-D	Burgers [†]	2.03 h	1.51 h
2-D	NS_TG [‡]	3.38 h	2.51 h
	NS_random [‡]	3.40 h	2.53 h

G Ablation experiments

We did the ablation experiments on diffusion equation Eq. (29) with $N = 4$ on the hyperparameter domain $\alpha = \{0, 1, 2, 3, 4\}$, $\beta = \{0, 1, 2, 3, 4\}$, $\epsilon = \{1, 10^{-1}, 10^{-2}, 10^{-3}, 10^{-4}, 10^{-5}, 10^{-6}\}$. The best hyperparameter for WL is $\epsilon = 10^{-5}$, and the corresponding error is $1.58 \times 10^{-6} \pm 6.94 \times 10^{-7}$ (see Table 9); The best hyperparameter for SI is $\alpha = 3, \beta = 0$, and the corresponding error is $1.73 \times 10^{-6} \pm 1.41 \times 10^{-6}$ (see Table 10); The best hyperparameter for combination of SI and WL is $\alpha = 1, \beta = 0, \epsilon = 10^{-5}$, and the corresponding error is $2.14 \times 10^{-6} \pm \times 10^{-7}$.

Table 9: Ablation of WL

ϵ	relative error
1.0	$1.25 \times 10^{-4} \pm 6.26 \times 10^{-5}$
10^{-1}	$8.85 \times 10^{-5} \pm 5.79 \times 10^{-5}$
10^{-2}	$1.23 \times 10^{-4} \pm 7.21 \times 10^{-5}$
10^{-3}	$4.40 \times 10^{-5} \pm 1.54 \times 10^{-5}$
10^{-4}	$7.13 \times 10^{-6} \pm 9.40 \times 10^{-7}$
10^{-5}	$1.58 \times 10^{-6} \pm 6.94 \times 10^{-7}$
10^{-6}	$8.15 \times 10^{-6} \pm 4.42 \times 10^{-6}$

Table 10: Ablation of SI

α/β	0	1	2	3
0	$8.94 \times 10^{-6} \pm 5.33 \times 10^{-6}$	$2.28 \times 10^{-6} \pm 1.62 \times 10^{-6}$	$9.63 \times 10^{-6} \pm 1.04 \times 10^{-5}$	$2.51 \times 10^{-6} \pm 2.18 \times 10^{-6}$
1	$3.54 \times 10^{-6} \pm 2.51 \times 10^{-6}$	$5.78 \times 10^{-6} \pm 2.09 \times 10^{-6}$	$4.94 \times 10^{-6} \pm 5.26 \times 10^{-6}$	$2.29 \times 10^{-6} \pm 1.38 \times 10^{-6}$
2	$3.52 \times 10^{-5} \pm 3.43 \times 10^{-5}$	$6.43 \times 10^{-6} \pm 7.40 \times 10^{-6}$	$9.31 \times 10^{-6} \pm 1.18 \times 10^{-5}$	$3.06 \times 10^{-5} \pm 2.96 \times 10^{-5}$
3	$1.73 \times 10^{-6} \pm 1.41 \times 10^{-6}$	$3.51 \times 10^{-6} \pm 3.47 \times 10^{-6}$	$9.14 \times 10^{-6} \pm 8.17 \times 10^{-6}$	$5.74 \times 10^{-6} \pm 4.07 \times 10^{-6}$

H Details of spectral method

Since the analytical solutions to the 1-D Burgers equation Eq. (36) as well as the 2-D heat equation Eq. (33) and NS equation Eq. (37) with random initialization are difficult to obtain, we developed in-house spectral method codes to provide the corresponding numerical solutions instead.

Specifically, the 1-D Burgers equation Eq. (36) in frequency space is

$$\hat{u}_t = -\nu k^2 \hat{u} - \mathcal{F}[uu_x], \quad k \in [-N/2, N/2 - 1], t \in [0, T]. \quad (49)$$

And the time derivative \hat{u}_t can be approximated by the optimal third-order total variation diminishing Runge-Kutta scheme [44], which has the following explicit discrete form:

$$\begin{aligned} \hat{u}_1 &= \hat{u}(t, k) - \Delta t \left\{ \nu k^2 \hat{u}(t, k) + \mathcal{F} \left[\mathcal{D} \left[\mathcal{F}^{-1} [\hat{u}(t, k)] \cdot \mathcal{F}^{-1} [ik\hat{u}(t, k)] \right] \right] \right\}, \\ \hat{u}_2 &= \frac{3}{4} \hat{u}(t, k) + \frac{1}{4} \hat{u}_1 - \frac{1}{4} \Delta t \left\{ \nu k^2 \hat{u}_1 + \mathcal{F} \left[\mathcal{D} \left[\mathcal{F}^{-1} [\hat{u}_1] \cdot \mathcal{F}^{-1} [ik\hat{u}_1] \right] \right] \right\}, \\ \hat{u}(t + \Delta t, k) &= \frac{1}{3} \hat{u}(t, k) + \frac{2}{3} \hat{u}_2 - \frac{2}{3} \Delta t \left\{ \nu k^2 \hat{u}(t, k) + \mathcal{F} \left[\mathcal{D} \left[\mathcal{F}^{-1} [\hat{u}_2] \cdot \mathcal{F}^{-1} [ik\hat{u}_2] \right] \right] \right\}, \end{aligned} \quad (50)$$

where Δt is the time step, \mathcal{D} is the dealiasing operator based on the Fourier smoothing method [42], and \hat{u}_1 and \hat{u}_2 are intermediate variables.

Besides, the 2-D heat equation Eq. (33) can be written in frequency space as

$$\hat{u}_t = -\epsilon (k_x^2 + k_y^2) \hat{u}, \quad \mathbf{k} = (k_x, k_y) \in [-N/2, N/2 - 1]^2, \quad t \in [0, T]. \quad (51)$$

The optimal third-order total variation diminishing Runge-Kutta scheme [44] can be employed for the time derivative \hat{u}_t , and the explicit discrete forms for \hat{u} are

$$\begin{aligned} \hat{u}_1 &= \hat{u}(t, \mathbf{k}) - \epsilon \Delta t (k_x^2 + k_y^2) \hat{u}(t, \mathbf{k}), \\ \hat{u}_2 &= \frac{3}{4} \hat{u}(t, \mathbf{k}) + \frac{1}{4} \hat{u}_1 - \frac{1}{4} \epsilon \Delta t (k_x^2 + k_y^2) \hat{u}_1, \\ \hat{u}(t + \Delta t, \mathbf{k}) &= \frac{1}{3} \hat{u}(t, \mathbf{k}) + \frac{2}{3} \hat{u}_2 - \frac{2}{3} \epsilon \Delta t (k_x^2 + k_y^2) \hat{u}_2. \end{aligned} \quad (52)$$

As for the 2-D NS equation Eq. (37), the second-order Adams-Bashforth scheme [23] is applied to the time discretization, and the explicit discrete system becomes

$$\begin{aligned} \hat{\mathbf{u}}(t + \Delta t, \mathbf{k}) &= e^{(-\nu|\mathbf{k}|^2\Delta t)} \left(1 - \frac{\mathbf{k}\mathbf{k}\cdot}{|\mathbf{k}|^2} \right) \left[\frac{3\Delta t}{2} \hat{\mathbf{N}}(t, \mathbf{k}) - \frac{\Delta t}{2} e^{(-\nu|\mathbf{k}|^2\Delta t)} \hat{\mathbf{N}}(t - \Delta t, \mathbf{k}) - \hat{\mathbf{u}}(t, \mathbf{k}) \right], \\ \hat{\mathbf{N}}(t, \mathbf{k}) &= \mathcal{F} [\mathcal{D} [\mathcal{F}^{-1} [i\mathbf{k} \times \hat{\mathbf{u}}(t, \mathbf{k})] \times \mathcal{F}^{-1} [\hat{\mathbf{u}}(t, \mathbf{k})]]], \\ \hat{\mathbf{N}}(t - \Delta t, \mathbf{k}) &= \mathcal{F} [\mathcal{D} [\mathcal{F}^{-1} [i\mathbf{k} \times \hat{\mathbf{u}}(t - \Delta t, \mathbf{k})] \times \mathcal{F}^{-1} [\hat{\mathbf{u}}(t - \Delta t, \mathbf{k})]]], \end{aligned} \quad (53)$$

where \mathcal{D} is the dealiasing operator based on the Fourier smoothing method [42].

In our calculations, the time steps for the aforementioned three discrete forms are chosen to be small enough to minimize the impact of numerical errors on the solutions.